Journal of Applied Fluid Mechanics, Vol. 18, No. 12, pp. 3053-3067, 2025.
Available online at www.jafmonline.net, ISSN 1735-3572, EISSN 1735-3645.
https://doi.org/10.47176/jafm.18.12.3557

Aerodynamics of UH-60 Helicopter-inlet Integration in Ground Effect

S. Yang[1], S. Sun[1], Z. Wu[1†], H. Zhou[1] and Y. Liu[2]

[1] *Nanjing University of Aeronautics and Astronautics, Nanjing, 210016, Jiangsu Province, China*
[2] *State Key Laboratory of Aerodynamics, Mianyang, 621000, Sichuan Province, China*

†*Corresponding Author Email: zhenlongwu@nuaa.edu.cn*

ABSTRACT

This paper describes a comprehensive numerical investigation into the aerodynamic characteristics of a full-scale UH-60 helicopter–inlet integrated flow field under the ground effect. The impact of both the internal and external flow parameters on the coupled flow field is analyzed, and the aerodynamic performance, streamline distributions, surface pressure, velocity fields, and vorticity magnitude are examined in detail. The numerical results demonstrate that the ground effect effectively reduces the flow losses within the air intake. Furthermore, the ground effect exhibits a significant attenuation in the presence of incoming flow, accompanied by substantial modifications in the three-dimensional flow field characteristics at the entrance of the intake. The internal parameters of the intake exert a substantial influence on the coupled flow field dynamics. This research elucidates the aerodynamic characteristics of the coupled interference in the near-ground flow fields across various operational conditions, providing valuable insights for helicopter flight operations under the ground effect.

Article History

Received April 6, 2025
Revised May 31, 2025
Accepted July 4, 2025
Available online October 6, 2025

Keywords:

Ground effect
Engine inlet
Aerodynamic characteristics
Helicopter
Computational fluid dynamics

1. INTRODUCTION

The ground effect (GE) is an aerodynamic phenomenon that occurs when an aircraft operates close to the ground. For helicopters, GE enhances lift, reduces the power requirements, and improves stability, particularly while hovering and during low-speed flight. However, transitions into or out of the GE region can induce instability, increasing the risks of an accident and posing significant challenges to flight safety (Matus-Vargas et al., 2021). When a helicopter is subject to GE, both the external flow field around the fuselage and the internal flow field within the intake exhibit distinct characteristics from those observed during out-of-GE operation. Therefore, in-depth research on the aerodynamic characteristics of the integrated coupled flow field of a helicopter is subject to GE is important, as it provides insights for optimizing rotorcraft performance in near-ground flight scenarios.

An understanding of the rotor near-ground interference flow field is a prerequisite for analysis of the coupled interference flow field considering the helicopter fuselage, rotor and intake. Many researchers have conducted numerical studies of the rotor near-ground interference flow field (Whitehouse et al., 2009; Kutz et al., 2013; Thomas et al., 2013; Han et al., 2021; Wu et al., 2024). The interaction between the rotor and the ground gives rise to a multitude of physical phenomena, including axial contraction, radial stretching, ground jets, and vortex pairs. The interaction between vortex pairs and the ground has been investigated experimentally (Wang et al., 2019; Chen et al., 2020). Yi et al. (2018) concluded that the single-side-wall deflection in convergent and divergent channel flows alters the merging rate and trajectories of the vortex pairs. In addition, the flow fields generated by rotors operating in GE are complex and unsteady. Milluzzo (2012), Milluzzo and Leishman (2017) studied the rotor flow field and tip vortex structures for different tip profiles. Their results revealed that forward protruding and swept-back tips significantly reduce the tip vortex strength and accelerate their dissipation. In recent years, significant advances have been made in the characterization of the complex flow field between the rotor and the ground, particularly through the development of advanced numerical methods. Suresh (2020) proposed a simple model for the flow field of a rotor in the presence of GE, in which a ring of point sources is positioned at the plane of the rotor, with the strength of the source distribution varying radially to simulate the induced velocity profile of the rotor disc. Silva et al. (2022) investigated the aerodynamic performance of a full helicopter hovering within and outside the range of GE using the multiple reference frame

NOMENCLATURE

C_T	thrust coefficient	Re	Reynolds number
$DC60$	total pressure distortion index	R	rotor radius
GE	ground effect	SCR	scavenge ratio
h	height	T	thrust
l	axial length of the intake	x	axial distance from the inlet
Ma	Mach number	ρ	air density
N	rotational speed	σ	total pressure recovery coefficient
p	local wall static pressure	ϕ	flow rate coefficient
P_0	incoming flow static pressure	Ω	rotation frequency
PIV	particle image velocimetry	Δt	time step

method coupled with high-order spatial accuracy. Pasquali et al. (2023) proposed a novel state-space wake inflow model that considers the effects of a stationary/moving ground beneath a hovering rotor; this formulation is particularly suitable for analyzing the impact of GE on helicopter rotors landing on ship decks.

In contrast to fixed-wing aircraft, helicopters produce a strong downwash flow from the rotor during normal operation, which impacts on both the helicopter fuselage and intakes. Kim and Komerath (1995) concluded that the rotor downwash wake and fuselage interference consists of two processes: a pre-collision process, where the trajectories of the wake vortices are affected by the fuselage and by the interference between the wake vortices and the fuselage boundary layer, and a viscosity-related collision process, which is difficult to model because the interaction between the wake vortices and the boundary layer leads to flow separation on the fuselage. Misté et al. (2012) analyzed the overall performance of the engine with helicopter pitot tube intakes, and observed a general increase in fuel consumption following the engine's mounting on the helicopter. This increase was observed to be 0.01% in hover mode and 0.3% while cruising. Full simulations based on the nested mesh approach are popular in the field of rotor/fuselage computational research. Tanabe et al. (2010) employed the nested mesh approach to solve the numerical flow field associated with helicopter fuselage/rotor interference, and simulated the detailed flow in the vicinity of the blades. However, the calculation of macroscopic quantities, such as rotor lift, are analogous to computational fluid dynamics (CFD) based on the momentum source model. At present, software is frequently employed to calculate the interference flow field. Ramasamy et al. (2015) used a building block approach to analyze the downwash and outwash characteristics of a tandem-rotor system close to the ground, and employed the Helios software to investigate how the single rotor of a helicopter is affected by the unsteady interference flow field characteristics induced by the ground. Rovere et al. (2020) used the HMB3 CFD software to study the interference flow field of a helicopter in the presence of the ground and buildings, and found that the near-ground interference induced significant ground jets around the rotor blades, while the non-stereotypical interference between rotor blade tip vortices and the ground significantly altered the near-ground flow field.

Previous research indicates that current studies on the aerodynamic coupling interference between the helicopter fuselage, rotor, intake, and ground have primarily focused on two coupling interference phenomena within the flow field structure. Therefore, this study focuses on the near-ground flow field under the coupled interference of a full-scale UH-60 helicopter–inlet integration using a simulation-based approach. The simulation method is initially validated through a series of experiments. The internal and external coupled flow fields of the helicopter at different hovering heights are then investigated, revealing the influence of GE. Subsequently, the influence of the coupled flow field is investigated by varying four parameters: the incoming flow velocity(V_0), core flow outlet Mach number (Ma), scavenge ratio (SCR), and rotor rotational speed. These studies are conducted at a height of 1R above the ground, where R is the rotor radius. The results from this study provide valuable insights into the internal and external coupled flow characteristics of helicopters under GE, offering a foundation for further research.

2. METHODOLOGICAL DESCRIPTION

2.1 Experimental Setup

Model rotor experiments were conducted in the Laboratory of Aviation and the Environment (LATE) at Nanjing University of Aeronautics and Astronautics (NUAA), China. The test cell (Fig. 1) has dimensions of approximately 15 m (length)×10 m (width)×3.5 m (height). The recirculation of the flow within the test cell was evaluated and determined to be minimal. A GE simulation platform and all essential flow measurement facilities were installed within the test cell. Figure 1 illustrates the rotor GE test platform developed by the research group. The platform is designed to accommodate varying rotor heights above the ground and rotational speeds, enabling the simulation of diverse test conditions. Pressure measurement probes are positioned on the ground surface to capture the pressure distribution induced by the rotor downwash flow. The ground plane measures 2 m × 2 m in size. The pressure was measured using an electronically scanned pressure system (ESP-64HD, PSI Inc.®), which exhibits an accuracy error of 0.05% at full scale. The system uses a single module with a measurement range of 1 psi (equivalent to 6.895 kPa).

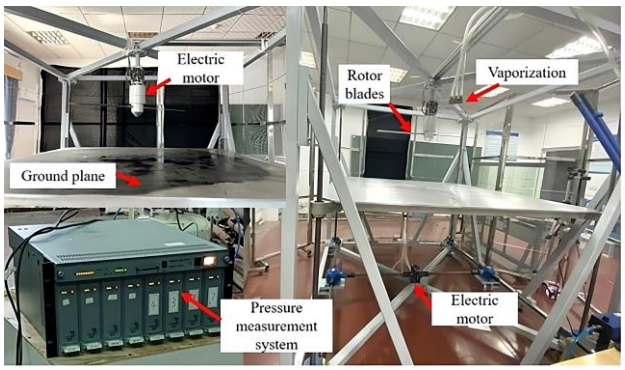

Fig. 1 Construction of the rotor GE test platform

The rotor blades were constructed from composite carbon fiber and featured a NACA0012 airfoil sectional profile. The blades were designed without taper or spanwise twist, having a chord length of 0.05 m, a radius of 0.5635 m, and a fixed collective pitch angle of 8°. The rotational speed ranged from 100–2500 rpm, resulting in a maximum tip speed of 146.4 m/s and a chord-based Reynolds number (Re) of 5,505,488. The test platform was equipped with modules for rotor load measurement and pitch angle regulation. Sensors were integrated into the rotor hub and controlled using the MET-V5 rotor test system software. The MET-V5 system provides several key functions, including throttle control, data collection and storage, automated testing, data analysis, and additional configurations such as system settings and safety protection.

The experimental setup accurately simulates the GE experienced by a helicopter while hovering. A screw mechanism was used to adjust the height of the ground plate, allowing for the simulation of different hover heights. Pressure probes installed on the ground plate measured the ground pressure induced by the downwash flow at various heights. The integration of the test platform with particle image velocimetry (PIV) measurements enabled the observation of vortex structure changes caused by the interaction of rotor tip vortices with the ground in the GE region. PIV also facilitated the measurement of ground vortices and the velocity distribution in the surrounding flow field.

2.2 Numerical Setup

2.2.1 Numerical Schemes

The commercial CFD software ANSYS FLUENT 2021 R1 was used to conduct the simulations. This software has been extensively employed in both external and internal flow simulations. The coupled interference near-ground flow field of a full-scale helicopter fuselage/rotor/intake is complex. When hovering and during low-speed forward flight, the impact of tip vortices on the fuselage can lead to significant aerodynamic interference, thereby altering the characteristics of the flow field. Therefore, simulations were conducted within an inertial coordinate system, employing the unsteady Reynolds-averaged Navier–Stokes (URANS) equations as the governing equations. The URANS equations were solved with the $k-\omega$ shear-stress transport turbulence model. The continuity and momentum equations of the URANS equations are respectively expressed as

$$\frac{\partial \rho}{\partial t}+\frac{\partial}{\partial x_i}\left(\rho u_i\right)=0 \tag{1}$$

$$\frac{\partial}{\partial t}\left(\rho u_i\right)+\frac{\partial}{\partial x_j}\left(\rho u_i u_j\right)=-\frac{\partial p}{\partial x_i}+\frac{\partial}{\partial x_j}\left[\mu\left(\frac{\partial u_i}{\partial x_j}+\frac{\partial u_j}{\partial x_i}-\frac{2}{3}\delta_{ij}\frac{\partial u_k}{\partial x_k}\right)\right]+\frac{\partial}{\partial x_j}\left(-\rho\overline{u_i'u_j'}\right) \tag{2}$$

where u_i, ρ and p represent the velocity component in the ith coordinate direction, density and pressure, respectively. δ_{ij} is the Kronecker delta function. $-\rho\overline{u_i'u_j'}$ is the Reynolds stress and which is modeled by the $k-\omega$ shear-stress transport turbulence model to close Eq. (2).

All simulation results presented in this paper correspond to the same instantaneous time. The time step was precisely calculated based on the angular velocity of rotor to maintain a constant 0.5°azimuthal increment per iteration. The corresponding values are: Δ t = 0.0003333 s (N = 250 rpm); Δ t = 0.0008332 s (N = 100 rpm). Twenty rotor revolutions were simulated before initiating the evaluations. The SIMPLEC scheme was used for pressure–velocity coupling iterations. The least-squares cell-based method was selected for gradient calculations. A second-order interpolation scheme was applied to the pressure term. All other terms, including density and turbulence, were discretized using the second-order upwind scheme.

2.2.2 Mesh and Boundary Condition

The UH-60 Black Hawk is highly representative of many helicopters. A simplified geometric model of the UH-60 from the Aviation Industry Corporation of China (AVIC) is presented in Fig. 2.

The grids generated for the flow field computations included the helicopter, intake, computational domain, and rotor blades. To ensure accuracy in the flow field simulations and computational efficiency, a rectangular computational domain with dimensions of 10R×10R×5R was selected, where R=8.18 m is the radius of the UH-60 rotor. The relative position between the helicopter and the ground was adjusted by modifying the computational domain. The grids of the rotor section were generated by

Fig. 2 UH-60 helicopter geometric model

Table 1 Variation of aerodynamic parameters for different mesh densities.

Parameter	Value					
	1600w		2400w		3100w	
	Left	Right	Left	Right	Left	Right
σ	0.9896	0.9875	0.9929	0.9903	0.9918	0.9916
DC60	0.0217	0.0338	0.0209	0.0348	0.0206	0.0342
C_T	0.01322		0.01347		0.01350	

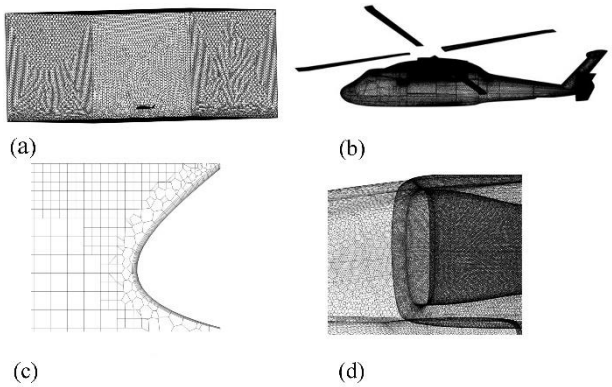

Fig. 3 Computational mesh of the integrated helicopter–intake mesh: (a) computational mesh, (b) helicopter mesh, (c) intake lip boundary layer mesh, (d) intake lip surface mesh

connecting the stationary and rotational domains using the "interface" condition. The number of grid cells of the flow region inside the intake and downwash region was gradually increased, and boundary layer grids were generated to capture the flow details. The computational mesh system for the helicopter components was configured with the following specifications: (1) The rotor surface contains 326,410 face elements with a maximum skewness of 0.66, featuring 20 boundary layers with a first-layer height of 5×10^{-6} m; (2) The fuselage surface consists of 409,307 face elements exhibiting a maximum skewness of 0.73, with 15 boundary layers and a first-layer height of 1×10^{-5} m; (3) The intake surface comprises 451,287 face elements demonstrating a maximum skewness of 0.68, and is configured with 20 boundary layers having a first-layer height of 1×10^{-5} m. The volume mesh employs unstructured hybrid tetrahedral-hexahedral elements throughout the computational domain, achieving a minimum orthogonal quality of 0.163.

Figure 3(a) depicts the meshes for the entire domain of the helicopter flight flow field calculations. The total number of polyhedral-hexahedral hybrid grid cells for the entire flow field is approximately 20 million. The airflow generates complex interference in the vicinity of the rotor, fuselage, and intake. Thus, the number of grid cells is increased in the region of the fuselage, where the flow field varies dramatically. Accordingly, larger grid cells are selected for the stationary fluid domain, while smaller grid cells are selected for the helicopter fuselage to adapt to the significant changes in the flow field. Figure 3(b) shows the global mesh of the helicopter fuselage. The inlet particle separator (IPS) is divided into two flow channels that use inertial force to separate sand and dust particles. The core flow is the clean airflow to the engine, and the scavenge flow is that which carries a large amount of sand and dust. Figure 3(c) provides an enlarged view of the boundary layer grids concentrated at the intake lip. The boundary layer grids near the intake wall capture the near-wall flow characteristics and improve the accuracy of the computational results. Figure 3(d) depicts the intake lip surface mesh. The internal structure of the intake undergoes a significant transformation, resulting in complex flow; consequently, the grid size is considerably smaller than that of the external flow field. The flow around the intake lip has a significant impact on the performance of the intake, so the number of grid cells must be increased to achieve a smooth and continuous profile.

2.2.3 Mesh Independence Examination

The mesh independence of the UH-60 helicopter model was analyzed. by considering three mesh densities: 16 million cells, 24 million cells, and 31 million cells. Table 1 compares the values of the total pressure distortion (DC60), the total pressure recovery (σ), and the rotor thrust coefficient (C_T) obtained from calculations performed on these three meshes. It can be observed that increasing the mesh density from 16 million to 24 million cells results in modest parameter variations: rotor thrust coefficient (C_T) increases by 1.89%, σ increases by 0.33% (left intake) and 0.28% (right intake), while DC60 decreases by 3.68% (left) and increases by 2.96% (right). Further refinement to 31 million cells shows significantly reduced variations: C_T increases by 0.22%, σ decreases by 0.11% (left) and increases by 0.13% (right), with DC60 decreasing by 1.44% (left) and 1.72% (right).

This analysis confirms that grid density effects remain within acceptable margins of error, warranting the adoption of the medium-density mesh (24 million cells) for all subsequent simulations. Figure 4 presents the Y+ distribution on the rotor surface at this density. The results demonstrate that Y+ is maintained within the optimal range around 1 across all regions of the rotor surface, which conclusively validates the effectiveness of the current boundary layer grid scheme for the rotor.

2.3 Methodological Validations

2.3.1 Validation of Rotor GE Aerodynamics.

To validate the accuracy of the simulation method for GE, a case study was conducted on the rotor model shown in Fig. 5(a). The numerical results of the rotor thrust coefficient were validated by the experimental values measured previously (Wu et al., 2024).

Figure 5(b) compares the experimental and numerical results for rotor thrust under varying rotor heights above ground at a rotational speed of 1500 rpm. As the rotor height above ground decreases, GE intensifies. Figure 5(b)

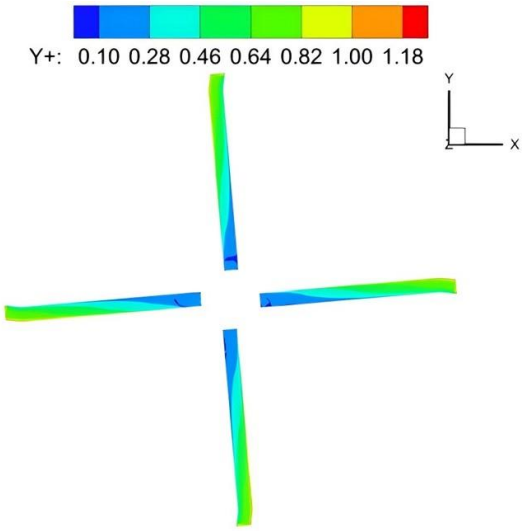

Fig. 4 Contours of Y+ value on the rotor blades

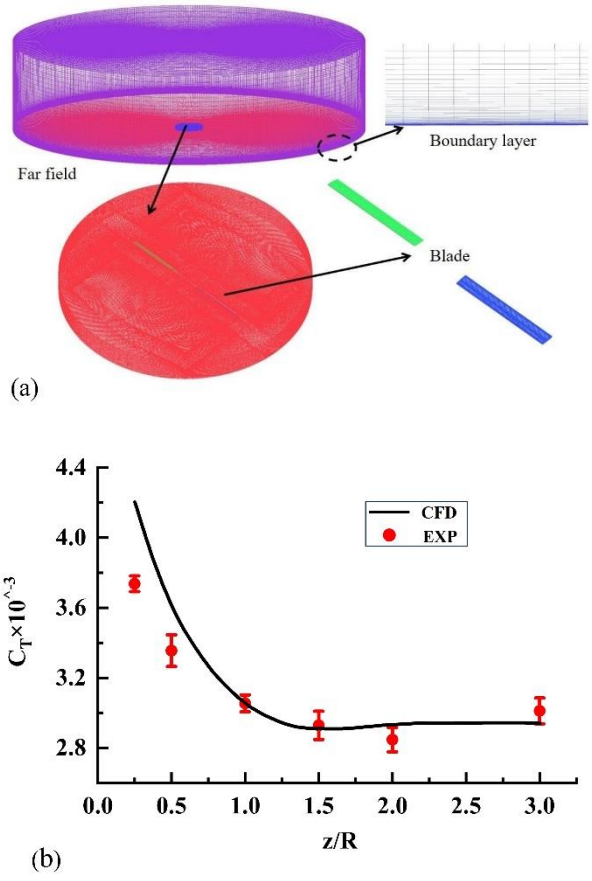

Fig. 5 (a) Rotor mesh model, (b) comparison of experimental and numerical results for the thrust coefficient with respect to rotor height above ground

demonstrates that when the rotor height above ground falls below 2*R*, the rotor thrust exhibits a significant increase with further reductions in height. Consequently, GE induces a measurable increase in rotor thrust performance. Although some discrepancies exist between the experimental and numerical results at lower heights, the overall trends observed in both datasets remain consistent.

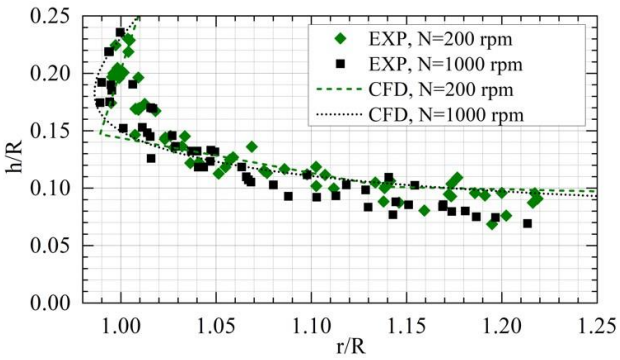

Fig. 6 Detached blade tip vortex positions for various rotational speeds and at h/R=0.25

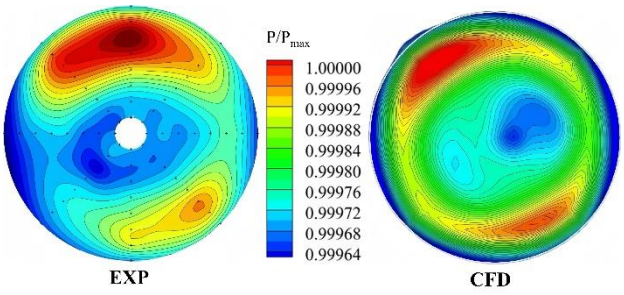

Fig. 7 Comparison of experimental and simulated ground pressure contours

Therefore, the method presented in this paper offers an accurate prediction of the influence of GE on the rotor thrust.

Figure 6 presents the comparison of experimental and numerical results for rotor blade tip vortex trajectories for various rotor speeds. These overlapping data points indicate the periodic displacements of the tip vortices produced by the periodicity of the locomotion of the two-bladed rotor. In addition, the tip vortex trajectories predicted by the CFD method fall well within the error range of the experimental measurements.

Figure 7 illustrates the experimental and simulated ground pressure contours at a height of 1R, with a rotor speed of 1500 rpm. The experimental and simulated results in Fig. 7 are in good agreement. Under the impact of downwash flow on the rotor disk, both results exhibit high-pressure regions near the outer area and low-pressure regions in the inner zone. A slight discrepancy appears in the low-pressure regions, with the experimental measurements showing lower pressure values compared with the computational results. This deviation primarily stems from two experimental constraints: (1) the pressure data were obtained through interpolation methods and (2) the absence of measurement points in the central region introduces unavoidable estimation errors.

2.3.2 Validation of IPS Internal-Flow Aerodynamics

To ascertain the viability of the intake flow field calculation method, the simulation method was validated on the particle separator model of the T700-GE-700 engine (Duffy & Shattuck, 1975). Figure 8 compares the

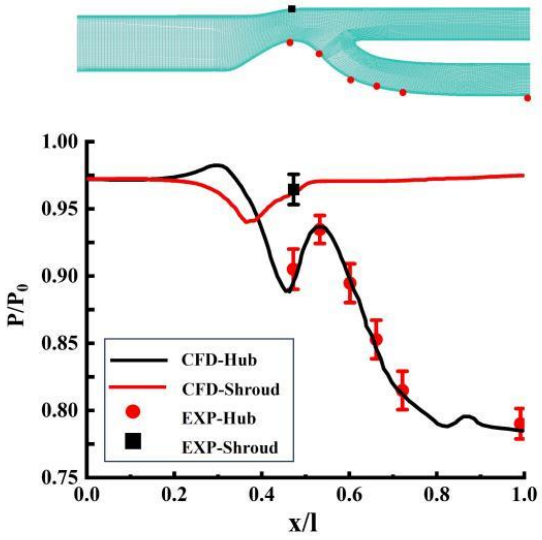

Fig. 8 Comparison of experimental and simulated pressure contours at the aerodynamic interface plane (AIP) of the inlet

wall static pressure results. The simulation results demonstrate a high degree of agreement with the experimental results, which indicates that the IPS simulations conducted in this study are capable of accurately representing the real flow.

2.4 Physical Parameter Definitions

The physical parameters used in this paper and their definitions are as follows:

Rotor thrust coefficient formula:

$$C_T = \frac{T}{\rho \pi R^2 (\Omega R)^2} \tag{3}$$

where T is the thrust generated by the rotation of the rotor, ρ is the air density, R is the radius of the rotor, and Ω is the rotation angular velocity of the rotor.

The total pressure recovery σ is defined as

$$\sigma = \frac{P_2^*}{P_0^*} \tag{4}$$

Where P_2^* is the average total pressure at the aerodynamic interface plane (AIP) between intake and engine and P_0^* is the freestream total pressure.

The total pressure distortion DC60 is defined as

$$\mathrm{DC60} = \frac{P_2^* - \overline{P}_{\min 60}^*}{q_{av}} \tag{5}$$

where $\overline{P}_{\min 60}^*$ is the minimum total pressure over all 60° section areas, and q_{av} is the average dynamic pressure at the AIP.

The SCR is defined as

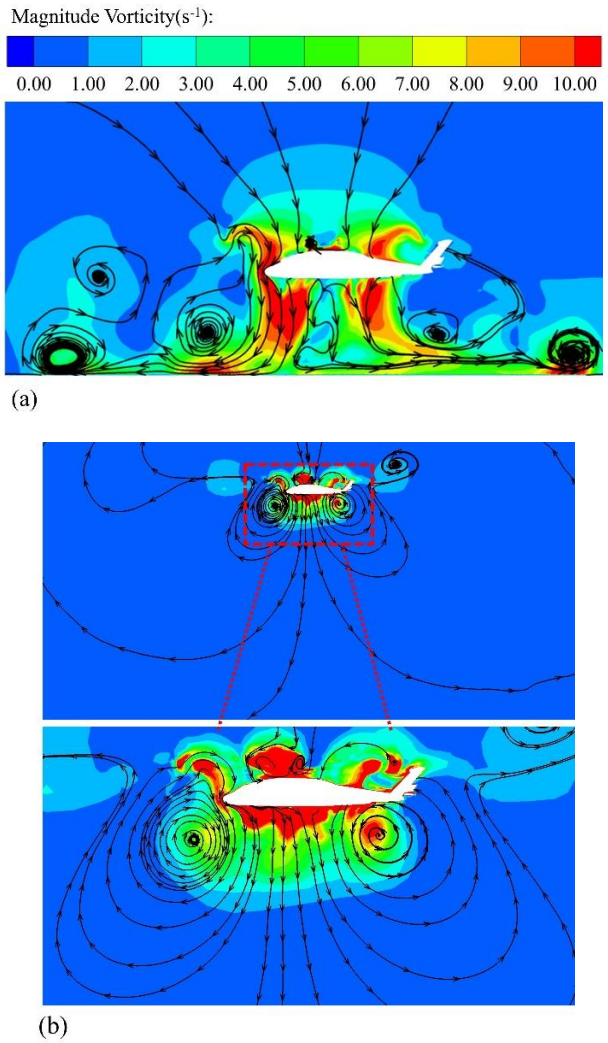

Fig. 9 Vorticity magnitude and streamline distributions in the symmetry plane at different hovering heights: (a) *h*=1*R*, (b) *h*=8*R*

$$SCR = \frac{m_s}{m_c} \tag{6}$$

Where m_s is the mass flow rate of the bypass duct and m_c is the mass flow rate of the engine duct.

3. Results and Discussion

All analyses in this study were performed using a 0° pitch angle as the baseline condition, with the exception of Section 3.6 where an 8° pitch angle configuration was employed.

3.1 Effect of GE

A flight height of 1R was chosen to study the impact of GE, primarily because real helicopters are equipped with landing gear. Reducing the flight height may lead to unsafe flight conditions. Figure 9 and Fig. 10 depict the distributions of vorticity magnitude and pressure for the helicopter at different hovering heights. The streamlines are based on the velocity components in the x, y and z directions within the inertial coordinate system. When the

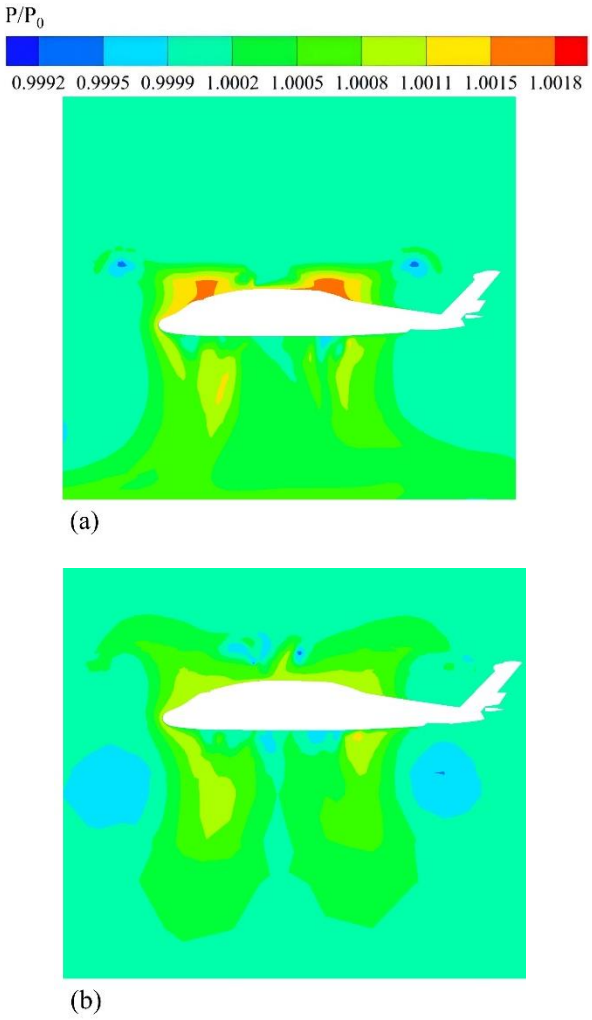

Fig. 10 Pressure distributions around the helicopter in the symmetry plane at different hovering heights: (a) *h*=1*R*, (b) *h*=8*R*

helicopter hovers at a height of 1*R*, the downwash flow generated by the rotor separates and moves laterally. The air descending towards the ground becomes constricted, resulting in the formation of vortices that induce an increase in pressure beneath the fuselage. This phenomenon creates a high-pressure zone that effectively elevates the fuselage. These vortices transition from axial to radial motion as they approach the ground. Upon reaching the ground surface, the vortices spread outward, resulting in radial stretching. This process leads to an increase in vorticity. The high-pressure zone located beneath the fuselage causes the vortices to ascend. Figure 9(b) illustrates the flow field structure of the helicopter in the symmetry plane without the ground effect. The downwash flow generated by the rotor creates recirculation zones around the fuselage.

Figure 11 shows the distributions of σ at the AIP at different hovering heights. The rotor rotates in a counterclockwise direction, resulting in an asymmetrical flow field on either side of the fuselage. Consequently, the flow characteristics of the intakes on both sides exhibit distinct differences. As the hovering height increases, the quantity of low-pressure zones decreases at the AIP.

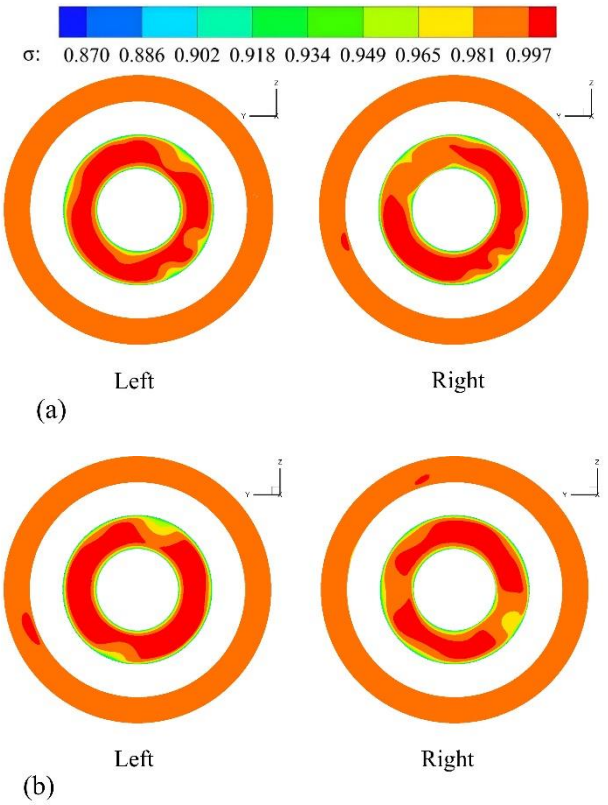

Fig. 11 Distributions of the total pressure recovery coefficient at the AIP at different hovering heights: (a) *h*=1*R*, (b) *h*=8*R*

Table 2 Aerodynamic parameters at the AIP at different hovering heights

Parameter	Value			
	L_{1R}	R_{1R}	L_{8R}	R_{8R}
σ	0.9904	0.9903	0.9833	0.9819
DC60	0.0229	0.0334	0.0366	0.0297

Table 2 presents the aerodynamic performance parameters at the AIP across various hovering heights. At the left and right AIPs, σ decreases as the hovering height increases. At the left AIP, DC60 increases by 59.8%, while at the right AIP, DC60 decreases by 11.1%

3.2 Effect of Incoming Flow Velocity

The height of the helicopter off the ground is designated as 1R, which will be applicable in the subsequent results. The cyclic and flapping angles can be neglected in the case of low-speed forward flight.

For fixed values of the core flow outlet Mach number (Ma=0.45), scavenge ratio (SCR=0.15), and rotor speed (250 rpm), the structure of the flow field is investigated for incoming flow velocities of V_0=0 m/s and 40 m/s.

Figure 12(b) reveals that although GE has not been entirely eliminated, it has been significantly weakened. A small fraction of downwash flow moves radially outward under the influence of the ground obstruction. This part of the downwash flow does not contact the ground, rather

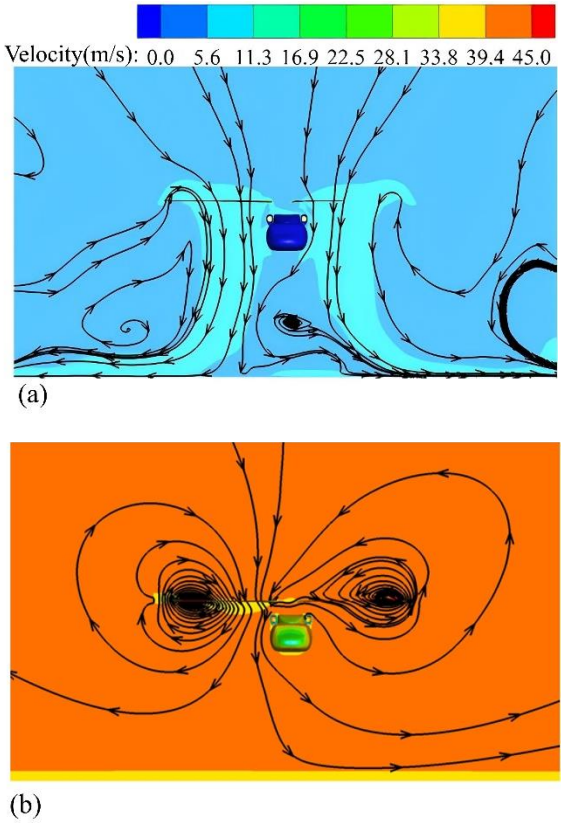

Fig. 12 Cross-sectional velocity and streamline distributions at the center of the fuselage flow field under different incoming flow velocities: (a) V_0=0m/s, (b) V_0=40m/s

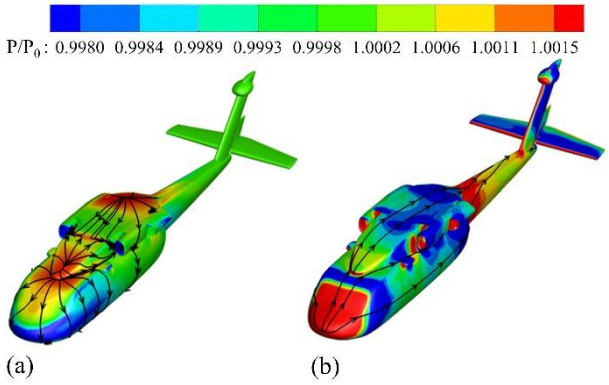

Fig. 13 Fuselage surface pressure and streamline distributions under different incoming flow velocities: (a) V_0=0m/s, (b) V_0=40m/s

impacts and bounces off the outside of the ground boundary layer (Lee et al., 2010) without penetrating the boundary layer of the ground surface.

Figure 13 illustrates the distributions of fuselage surface pressure and streamlines under different incoming flow conditions. When V_0=40 m/s, the streamlines extend continuously from the fuselage nose to the tail, aligning with the flow direction. At the front end of the fuselage, the airflow diverges radially from a point source, creating a high-pressure zone near the fuselage nose and a low-pressure zone on the rear side.

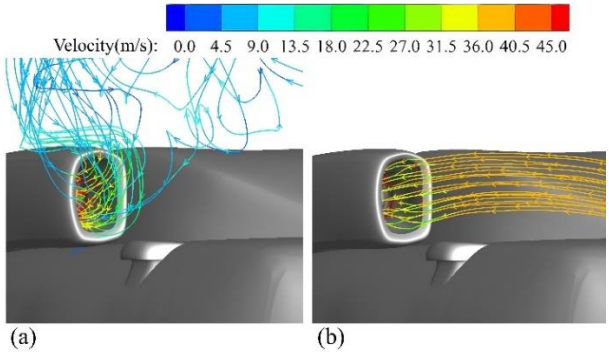

Fig. 14 Three-dimensional streamlines velocity distributions at the left intake for different incoming flow velocities: (a) V_0=0m/s, (b) V_0=40m/s

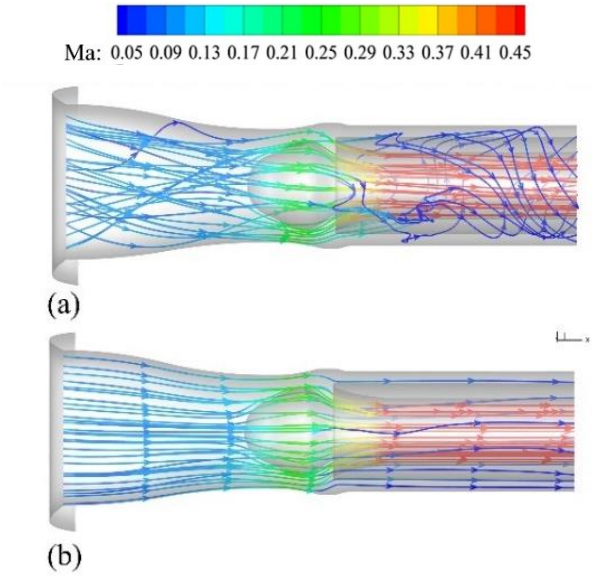

Fig. 15 Three-dimensional streamline velocity distributions in the left intake under different incoming flow velocities: (a) V_0=0m/s, (b) V_0=40m/s

Figure 14 illustrates the three-dimensional streamline velocity distributions at the left inlet. As V_0 increases, Ma at the intake outlet remains constant, and the flow rate is conserved. The cross-sectional area of the forward flow tube contracts, leading to a decrease in streamline velocity. The airflow at the inlet decelerates and the pressure increases, indicating that ϕ is less than 1.

Figure 15 shows the three-dimensional streamline distributions within the left intake. When V_0= 40m/s, the airflow streamlines inside the intake are relatively smooth in the axial direction, and the velocity gradient is reduced in the circumferential direction.

Figure 16 shows the distributions of σ at the AIP of the intake under different incoming flow conditions. When V_0= 40 m/s, σ at the AIP decreases; however, no distinct region of low total pressure recovery is observed. As V_0 increases, the friction with the intake wall increases, resulting in an increase in the flow loss within the intake; consequently, σ at the intake outlet decreases.

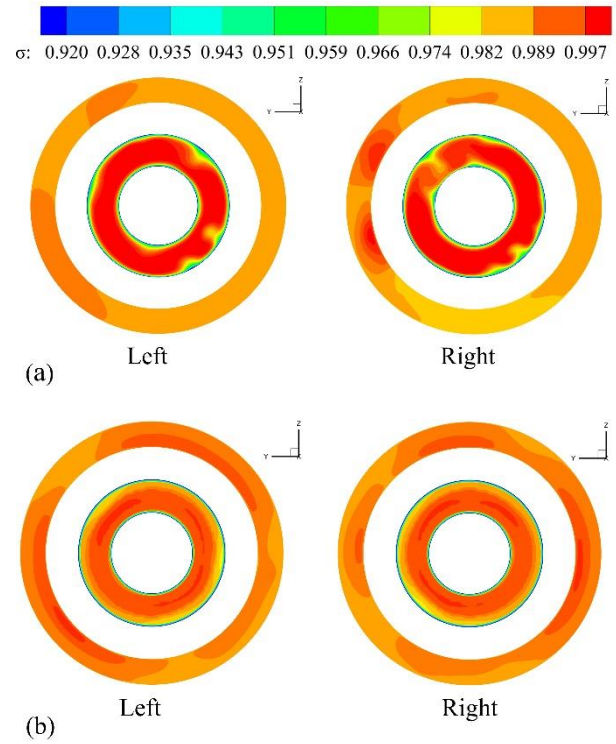

Fig. 16 Distributions of the total pressure recovery coefficient at the AIP under different incoming flow velocities: (a) V_0=0m/s, (b) V_0=40m/s

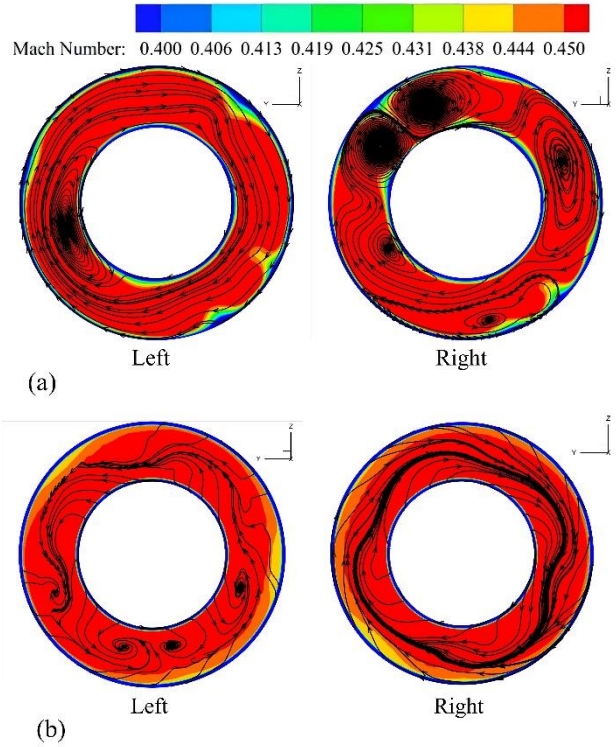

Fig. 17 Distributions of velocity and streamlines at the AIP under different incoming flow velocities: (a) V_0=0m/s, (b) V_0=40m/s

Figure 17 illustrates the velocity and streamline distributions at the AIP of the intake under varying incoming flow velocities. During hovering, there are more vortices at the AIP and large-scale vortices are present, which dominate in the total pressure distortion index at the AIP. During forward flight, the Ma distributions at the AIP become uniform, with minimal circumferential distortion. There are no large-scale vortices, and only some small-scale vortices are present at the left AIP.

Table 3 Aerodynamic parameters at the AIP under different incoming flow conditions

Parameter	Value			
	L_0	R_0	L_V	R_V
σ	0.9904	0.9903	0.98538	0.98537
DC60	0.0229	0.0334	0.01036	0.0096

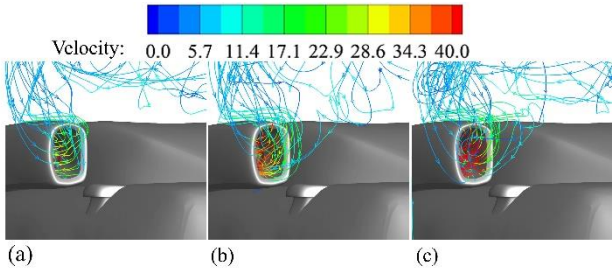

Fig. 18 Three-dimensional streamline velocity distributions at the left intake for different outlet Ma: (a) Ma=0.3, (b) Ma=0.45, (c) Ma=0.6

Table 3 presents the aerodynamic parameters at the AIP under different incoming flow conditions. As the V_0 increases, σ at the AIP decreases by 0.5%. Simultaneously, DC60 at the left intake decreases by 54.7%, and that at the right intake decreases by 71.3%, DC60 at the left AIP is greater than that at the right AIP under incoming flow conditions. This can be primarily attributed to the circumferential distortion induced by small-scale vortices.

3.3 Effect of Core Flow Outlet Ma

To explore the effect of Ma, the V_0 was fixed to 0 m/s, and the rotor speed and SCR were set to 250 rpm, and 0.15, respectively, while the core flow outlet Ma was successively set to 0.3, 0.45, and 0.6.

Figure 18 illustrates the three-dimensional streamline distributions at the intake lip. As the outlet Ma increases, the inlet flow velocity rises correspondingly, leading to an expanded influence on the upstream airflow at the inlet. Furthermore, the rotor downwash flow interference is enhanced, and a larger vortex forms above the nacelle.

Figure 19 illustrates the three-dimensional streamline velocity distributions within the left intake for different outlet Ma. As Ma increases, the deflection of streamlines in the forward section of the intake decreases, while the overall airflow velocity increases. However, the flow interference at the center body head intensifies, resulting in increased streamline disorganization.

The pressure and streamline distributions of the intake AIP are compared for different outlet Ma values in Fig. 20. It can be observed that as the outlet Ma increases, the pressure at the AIP decreases, the low-pressure region

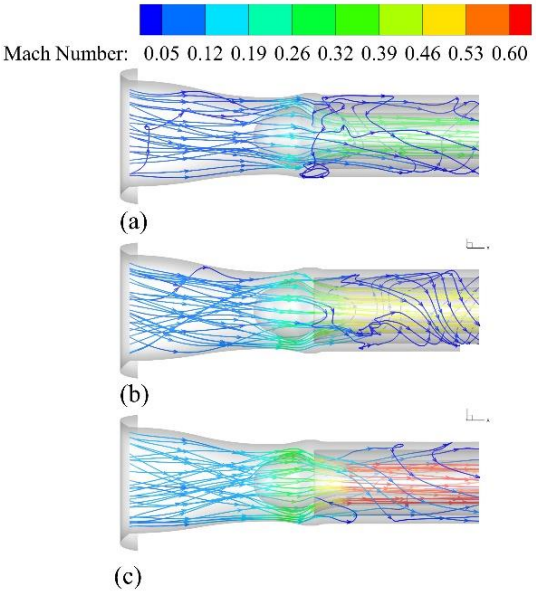

Fig. 19 Three-dimensional streamline velocity distributions of the left intake for different outlet Ma: (a) Ma=0.3, (b) Ma=0.45, (c) Ma=0.6

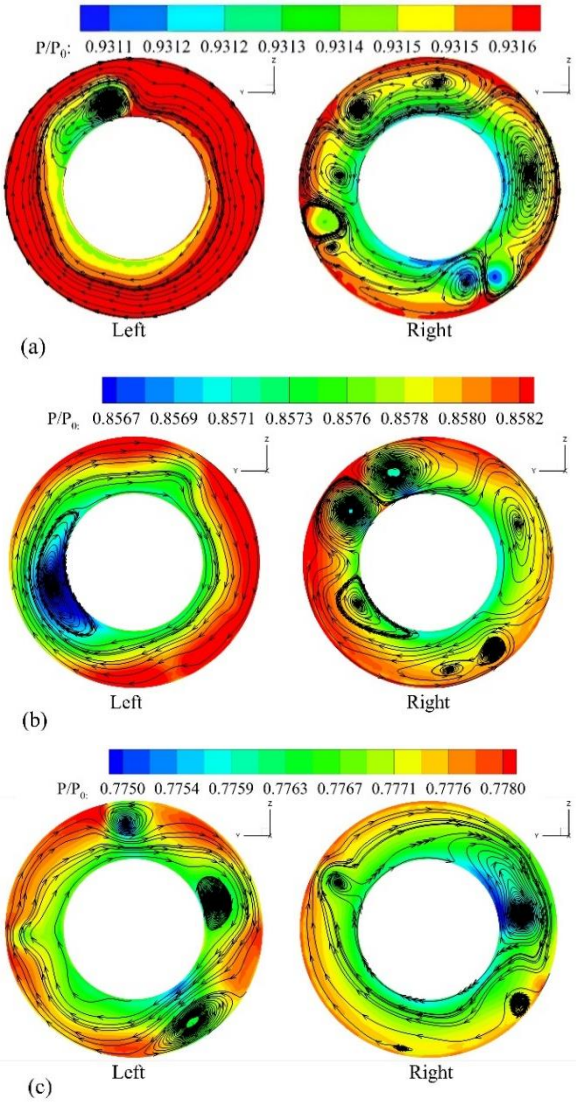

Fig. 20 Distributions of AIP pressure and streamline for different outlet Ma: (a) Ma=0.3, (b) Ma=0.45, (c) Ma=0.6

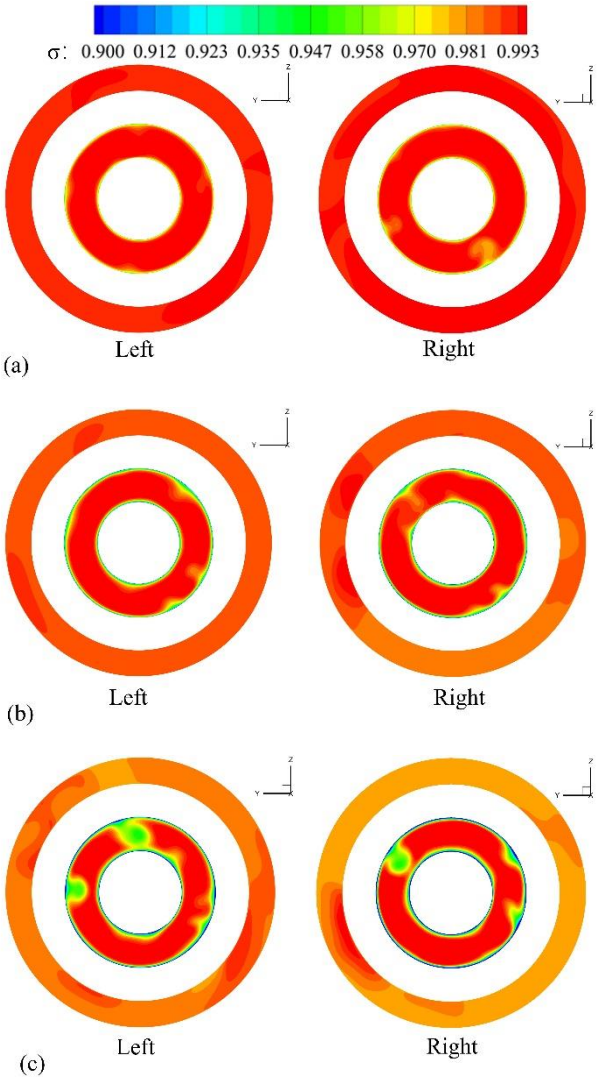

Fig. 21 Distributions of the total pressure recovery coefficient at the AIP for different outlet Ma: (a) Ma=0.3, (b) Ma=0.45, (c) Ma=0.6

expands, and the asymmetry of the flow field intensifies. Distinct secondary flow structures are evident between the left and right AIPs. The increase in the size of the left vortex is primarily attributed to the enhancement of interference between the inlet airflow and rotor downwash flow, as well as the enlargement of the vortex scale generated by the central body and the power output axis within the intake. Conversely, the reduction in size of the right vortex is due to the right intake's absorption of a significant number of vortices from both the fuselage boundary layer and the upper side of the nacelle at low Ma values. As the required flow rate for the intake increases, the expanded upstream flow tube absorbs a greater volume of undisturbed airflow, as well as some low-rotation airflow originating from the rotor center.

Figure 21 illustrates the distributions of σ at the AIP for different outlet Ma. As the outlet Ma increases, σ at the AIP decreases, and the low-pressure region near the separator expands. This phenomenon is attributed to the significant flow changes at the bifurcation plane as the airflow velocity increases, which intensifies the separator interference and generates strong flow disturbances.

Table 4 Aerodynamic parameters at the AIP for different Mach numbers

Parameter	Value					
	$L_{0.3}$	$L_{0.45}$	$L_{0.6}$	$R_{0.3}$	$R_{0.45}$	$R_{0.6}$
σ	0.995	0.9904	0.9816	0.9943	0.9903	0.9848
DC60	0.028	0.0229	0.0566	0.0401	0.0334	0.0399

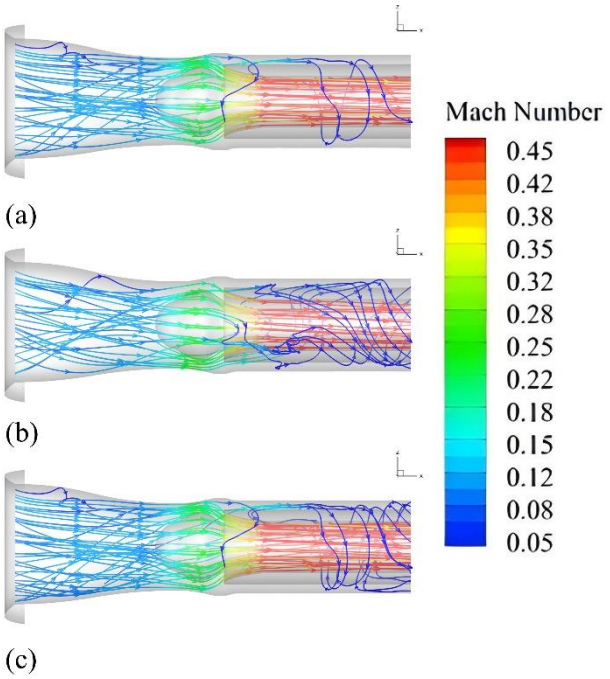

Fig. 22 Three-dimensional streamlines velocity distributions in the left intake for different SCR values: (a) SCR=0.05, (b) SCR=0.15, (c) SCR=0.3

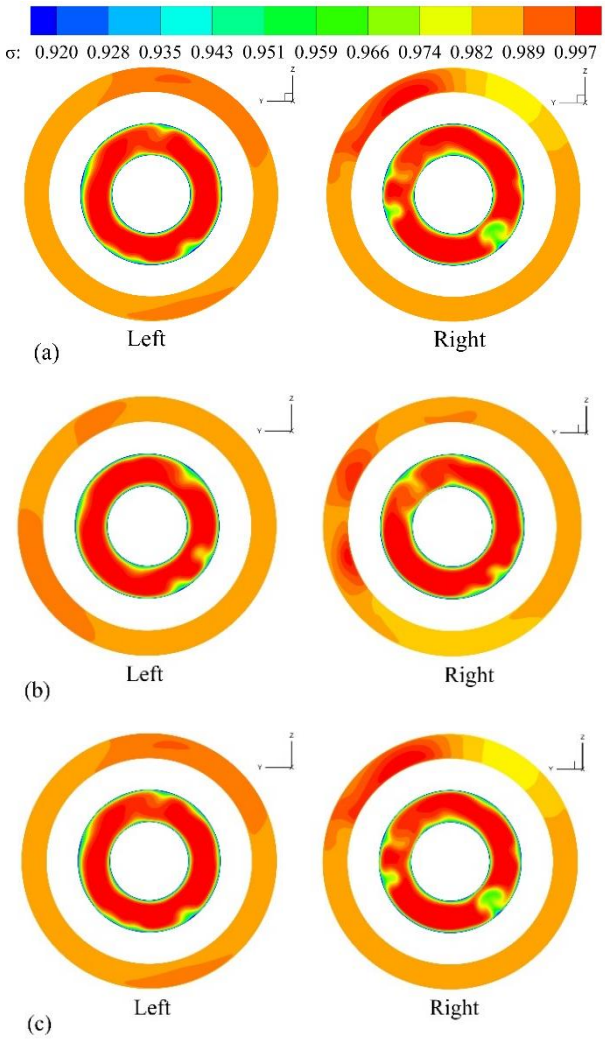

Fig. 23 Distributions of the total pressure recovery coefficient at the AIP for different SCR values: (a) SCR=0.05, (b) SCR=0.15, (c) SCR=0.3

Table 4 presents the aerodynamic performance parameters at the AIP for different outlet Ma. When Ma reaches 0.6, σ at the left intake outlet has decreased by approximately 1.35% compared with the value when Ma=0.3, while that at the right intake outlet has decreased by approximately 0.96%. The reduction is primarily attributed to the increase in Ma. The upstream airflow is influenced by the downstream low-pressure region, which accelerates the airflow in advance and results in increased friction loss. Furthermore, the rise in airflow velocity within the intake enhances the interference with the center body and separator, intensifies the cyclone effect, and contributes to higher overall losses. DC60 exhibits a fluctuating trend, characterized by an initial decrease followed by an increase. At low Ma, DC60 is higher at the right AIP than at the left AIP. Conversely, at Ma=0.6, DC60 at the right AIP is lower than that at the left AIP. This is attributed to the increasing inhomogeneity of the airflow at the left AIP with rising Ma, while both the inhomogeneity and circumferential distortion of the airflow at the right AIP decrease.

3.4 Effect of SCR

The effects of setting SCR to 0.05, 0.15, and 0.3 on the flow field structure are now investigated for a constant core flow rate and rotor speed. Figure 22 illustrates the three-dimensional streamline velocity distributions within the left intake under the different SCR conditions. The flow state in the front section of the intake remains relatively consistent for the different SCR values, while the divergence in the flow field downstream of the bifurcation channel becomes more pronounced. At SCR values of 0.05 and 0.3, the streamlines in the scavenge passage exhibit greater curvature, forming a circulation within the annulus. In contrast, at SCR= 0.15, the streamlines are less curved, resulting in a weaker circulation.

Figure 23 illustrates the distributions of σ at the AIP for different SCR values. The contours of the left AIP

Table 5 Aerodynamic parameters at the AIP for different SCR values

Parameter	Value					
	$L_{0.05}$	$L_{0.15}$	$L_{0.3}$	$R_{0.05}$	$R_{0.15}$	$R_{0.3}$
σ	0.9906	0.9904	0.9885	0.989	0.9903	0.9873
DC60	0.02267	0.02299	0.02763	0.02478	0.03339	0.0624

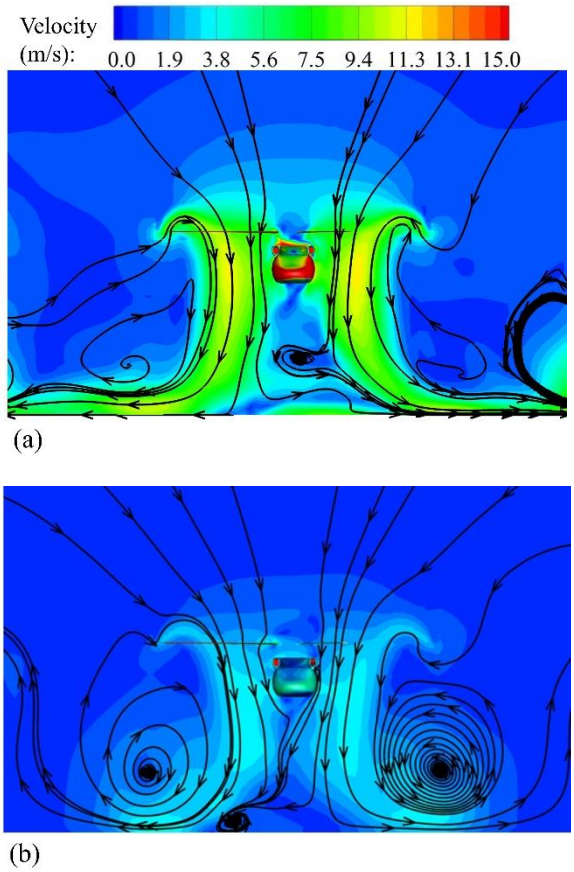

Fig. 24 Cross-sectional velocity and streamline distributions at the center of the airframe flow field for different rotational speeds: (a) 250 rpm, (b) 100 rpm

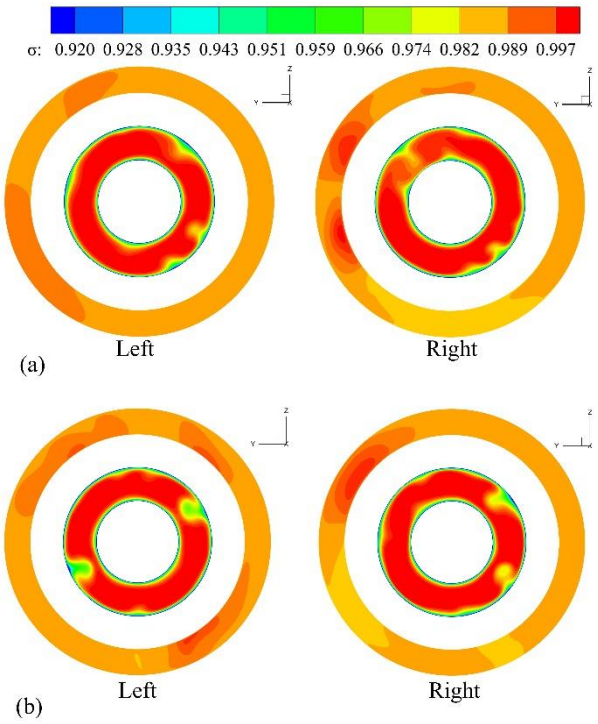

Fig. 25 Distributions of the total pressure recovery coefficient at the AIP for different rotational speeds: (a) 250 rpm, (b) 100 rpm

exhibits minimal variation, while the low-pressure region of the right AIP displays a gradual decrease followed by an increase as SCR increases.

Table 5 presents the aerodynamic performance parameters at the AIP for different SCR values. As SCR increases, σ at the left AIP decreases by 0.2%, while that at the right AIP initially increases by 0.13% and then decreases by 0.3%. Subsequently, DC60 increases by 21.9% at the left intake and by 151.8% at the right intake. It can be concluded that both excessively high and low SCR values adversely affect the intake's performance.

3.5 Effect of Rotational Speed

V_0 was maintained at 0 m/s and Ma was fixed at 0.45 while the effect of rotor speeds of 250 rpm and 100 rpm on the flow field structure was investigated. Figure 24 illustrates the cross-sectional velocity and streamline distributions at the center of the fuselage flow field for different rotational speeds. As the rotational speed decreases, the rotor-induced velocity of the airflow is reduced, and the disk work capacity decreases. Additionally, the rotor downwash flow velocity declines, the radial extent of the ground vortex contracts, and the low-speed flow region beneath the fuselage shrinks.

Figure 25 shows the distributions of σ at the intake AIP for different rotational speeds. As the rotor speed decreases, the region of low total pressure, which is situated on the side of the separator position, expands in size.

Table 6 presents the aerodynamic parameters of the intake for different rotational speeds. As the rotational speed decreases, σ at the left AIP decreases by 0.08%, while that at the right AIP decreases by 0.03%. Additionally, DC60 at the left AIP increases by 34.8%, whereas that at the right AIP decreases by 10.2%.

3.6 Effect of the Rotor Collective Pitch Angle

The effect of rotor collective pitch angles of 0° and 8° on the flow field structure was investigated by setting V_0=0 m/s and fixing the rotor speed to 250 rpm. Figure 26 shows that the rotor downwash velocity increases significantly at the higher pitch angle, while the radial expansion range of the ground vortex exhibits a noticeable enlargement.

Table 6 Aerodynamic parameters at the AIP for different rotational speeds

Parameter	Value			
	L_{250rpm}	R_{250rpm}	L_{100rpm}	R_{100rpm}
σ	0.9904	0.9903	0.9896	0.99
DC60	0.023	0.0334	0.031	0.03

Table 7 Aerodynamic parameters at the AIP for different rotor collective pitch angles

Parameter	Value			
	L (0°)	R (0°)	L (8°)	R (8°)
σ	0.9904	0.9903	0.9929	0.9903
DC60	0.023	0.0334	0.0209	0.0348

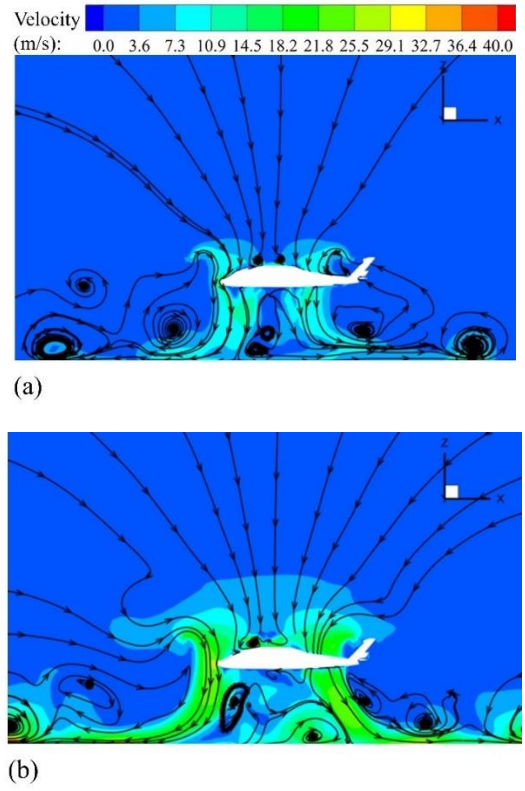

Fig. 26 Velocity and streamline distributions in the symmetry plane for different rotor collective pitch angles: (a) 0°, (b) 8°

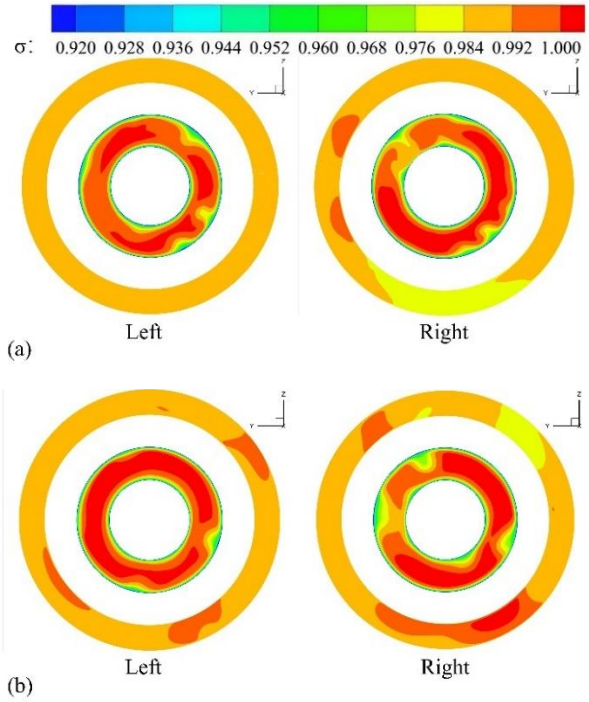

Fig. 27 Distributions of the total pressure recovery coefficient at the AIP for different rotor collective pitch angles: (a) 0°, (b) 8°

Figure 27 shows the distributions of σ at the intake AIP for different rotor collective pitch angles. As the rotor collective pitch angle increases, the low-pressure zone on the left AIP contracts, whereas the right counterpart enlarges.

Table 7 presents the aerodynamic performance parameters at the AIP for different rotor collective pitch angles. As the collective pitch angle increases, σ at the left AIP increases by 0.25%, while the value at the right AIP remains unchanged. A subsequent 9.1% reduction in DC60 is observed at the left intake, contrasted with a 4.2% increase at the right intake.

4. CONCLUSION

This study has investigated the structure of the coupled helicopter/rotor/intake interference within a GE flow field using a numerical approach. The following conclusions can be drawn from our results.

4. CONCLUSION

This study has investigated the structure of the coupled helicopter/rotor/intake interference within a GE flow field using a numerical approach. The following conclusions can be drawn from our results.

(1) The downwash flow under GE initially contracts radially before subsequently expanding near the ground. At both the left and right AIPs, σ decreases as the hovering height increases. Aerodynamic analysis confirms that GE substantially enhances engine intake performance. During low-altitude hovering operations, the ground-induced flow interaction promotes radial contraction of the downwash field, creating a favorable high-pressure zone in the intake region. This aerodynamic phenomenon demonstrates that appropriately increasing rotor diameter

can enhance the performance of intake, as a larger disk area expands the beneficial ground effect zone.

(2) The coupled helicopter/rotor/intake flow field at V_0=40 m/s is different from that in the hovering state. The rotor GE is greatly weakened, the ground vortices disappear, and the three-dimensional flow field at the intake inlet is altered. At the intake, σ decreases by 0.5%. At the left and right AIPs, DC60 decreases by approximately 54.7% and 71.3%, respectively.

(3) As the core flow outlet Ma increases, the airflow velocity at the inlet of the intake increases, DC60 increases, and σ at the AIP decreases. The distortion index decreases and then increases by about 146%.

(4) As SCR increases, σ at the left intake decreases by 0.2%, while that at the right intake initially increases by 0.13% and then decreases by 0.3%. Subsequently, DC60 increases by 21.9% at the left intake and by 151.8% at the right intake. These results demonstrate that SCR significantly influences the performance of the intake. Future studies should focus on parameter optimization to determine the optimal SCR for this type of intake.

(5) As the rotor speed decreases, σ at the left AIP decreases by 0.08%, while that at the right AIP decreases by 0.03%. Simultaneously, DC60 at the left AIP increases by 34.8%, whereas that at the right AIP decreases by 10.2%.

(6) The rotor downwash velocity increases significantly at the higher pitch angle, while the radial expansion range of the ground vortex exhibits a noticeable enlargement.

ACKNOWLEDGEMENTS

This research was partially supported by the open subject of State Key Laboratory of Aerodynamics of China under grant RAL202402-7 and the National Science and Technology Major Project under grant HT-J2019-V-0004-0095.

CONFLICT OF INTEREST

The authors declare that they have no conflict of interest in this work.

AUTHORS CONTRIBUTION

Shuoyu Yang: Methodology, Software, Validation, Investigation, Data curation, Writing of the Original Draft; **Shun Sun:** Supervising, Methodology, Validation, Writing of the Final Manuscript; **Haoyu Zhou:** Software, Validation, Writing of the Original Draft; **Zhenlong Wu:** Supervising, Methodology, Conceptualization, Review and Editing, Project Administration; **Yakui Liu:** Data curation.

REFERENCES

Chen, Q., Hu, T., Liu, P., Liu, Y., Qu, Q., Guo, H., & Akkermans, R. A. D. (2020). Experiments on asymmetric vortex pair interaction with the ground. *Experiments in Fluids*, *61*(6), 1-22. https://doi.org/10.1007/s00348-020-02987-7

Duffy, R. J., & Shattuck, B. F. (1975). *Integral engine inlet particle separator.* (USAAMRDL-TR-75-31B). U. S. A. A. M. R. a. D. Laboratory.

Han, H., Xiang, C., Xu, B., & Yu, Y. (2021). Experimental and computational investigation on comparison of micro-scale open rotor and shrouded rotor hovering in ground effect. *Proceedings of the Institution of Mechanical Engineers, Part G: Journal of Aerospace Engineering*, *235*(5), 553-565. https://doi.org/10.1177/0954410020949292

Kim, J. M., & Komerath, N. M. (1995). Summary of the interaction of a rotor wake with a circular cylinder. *AIAA Journal*, *33*(3), 470-478. https://doi.org/10.2514/3.12600

Kutz, B. M., Bensing, F., Keßler, M., & Krämer, E. (2013). CFD calculation of a helicopter rotor hovering in ground effect. *Notes on Numerical Fluid Mechanics and Multidisciplinary Design*, *121*, 297-304. https://doi.org/10.1007/978-3-642-35680-3_36

Lee, T. E., Leishman, J. G., & Ramasamy, M. (2010). Fluid dynamics of interacting blade tip vortices with a ground plane. *Journal of the American Helicopter Society*, *55*(2), 022005. https://doi.org/10.4050/JAHS.55.022005

Matus-Vargas, A., Rodriguez-Gomez, G., & Martinez-Carranza, J. (2021). Ground effect on rotorcraft unmanned aerial vehicles: a review. *Intelligent Service Robotics*, *14*(1), 99-118. https://doi.org/10.1007/s11370-020-00344-5

Milluzzo, J. I. (2012). *The effect of blade tip shapes on rotor in-ground-effect aerodynamics* [Master's thesis, University of Maryland]. https://www.proquest.com/dissertations-theses/effect-blade-tip-shapes-on-rotor-ground/docview/1197735243/se-2?accountid=16605

Milluzzo, J. I., & Leishman, J. G. (2017). Vortical sheet behavior in the wake of a rotor in ground effect. *AIAA Journal*, *55*(1), 24-35. https://doi.org/10.2514/1.J054498

Misté, G. A., Nibale, T., Garavello, A., & Benini, E. (2012). *Assessment of the engine installation performance of a redesigned tilt-rotor intake system.* American Helicopter Society 68th Annual Forum, Fort Worth, Texas.

Pasquali, C., Gennaretti, M., Bernardini, G., & Serafini, J. (2023). State-space dynamic inflow modelling for hovering rotors in fixed and moving-ground effect. *Aerospace Science and Technology*, *140*, 108414. https://doi.org/10.1016/j.ast.2023.108414

Ramasamy, M., Potsdam, M., & Yamauchi, G. K. (2015, May 21-23). *Measurements to Understand the flow mechanisms contributing to tandem-rotor outwash.* AHS 71st Annual Forum, Virginia Beach, VA, United States. https://doi.org/10.4050/F-0071-2015-10100

Rovere, F., Barakos, G. N., & Steijl, R. (2020). *CFD analysis of a micro-rotor in ground effect*. AIAA Scitech 2020 Forum, Orlando, FL, United States. https://doi.org/10.2514/6.2020-1793

Silva, P. A. S. F., Tsoutsanis, P., & Antoniadis, A. F. (2022). Numerical investigation of full helicopter with and without the ground effect. *Aerospace Science and Technology, 122*, 107401. https://doi.org/10.1016/j.ast.2022.107401

Suresh, A. (2020). A Simple model of rotor upwash in ground effect. *AIAA Scitech 2020 Forum*. Orlando, FL, United States. https://doi.org/10.2514/6.2020-1999

Tanabe, Y., Otani, I., & Saito, S. (2010). *Validation of computational results of rotor/fuselage interaction analysis using rFlow3D code*. Japan Aerospace Exploration Agency Tokyo, Japan. https://www.proquest.com/other-sources/validation-computational-results-rotor-fuselage/docview/756657804/se-2?accountid=16605

Thomas, S., Amiraux, M., & Baeder, J. D. (2013). Modeling the two-phase flowfield beneath a hovering rotor on graphics processing units using a FVMRANS hybrid methodology. *21st AIAA Computational Fluid Dynamics Conference*, San Diego, CA, United States. https://doi.org/10.2514/6.2013-2853

Wang, Y., Liu, P., Hu, T., Qu, Q., Chen, Q., & Akkermans, R. (2019). Experimental Investigations on the interaction of the single/co-rotating vortex with the ground. *AIAA Journal*, *57*(2), 499-512. https://doi.org/10.2514/1.J057140

Whitehouse, D., Yu, J., Gilmore, P., Dorsett, M., McClure, K., & SAIC, R. A. (2009, May 27–29). *A high fidelity brownout model for real-time flight simulations and trainers* American Helicopter Society 65th Annual Forum, Grapevine, TX. https://citeseerx.ist.psu.edu/document?repid=rep1&type=pdf&doi=1e1f2b575f05efac5ea27d6ca65d61127976c267

Wu, Z., Zhang, T., Tan, H., Zhou, H., Chen, W., & Xie, M. (2024). Hovering rotor aerodynamics in extreme ground effect. *Chinese Journal of Aeronautics*, *37*(7), 204-219. https://doi.org/10.1016/j.cja.2024.02.020

Yi, Y., Liu, P., Hu, T., Qu, Q., & Akkermans, R. A. D. (2018). Experimental investigations on co-rotating vortex pair merger in convergent/divergent channel flow with single-side-wall deflection. *Experiments in Fluids*, *59*(12), 1-18. https://doi.org/10.1007/s00348-018-2643-8